J Adv Ceram

Research Article

Densified micro-zone molten salt method for scale-up synthesis of high-entropy ceramic powders

Yongxin Wang[1,†], Ling Zhang[4,†], Tianyu Xue[1], Yabo Gao[1], Hang Li[1], Huicong Lei[1], Zhong Huang[1,2,✉], Jinhui Cao[3,✉], Haijun Zhang[1], Shaowei Zhang[4,✉]

Cite this article: Wang Y, Zhang L, Xue T, et al. *J Adv Ceram* 2026, **15**(4): 9221273. https://doi.org/10.26599/JAC.2026.9221273

ABSTRACT: Molten salt methods have been widely used in the synthesis of high-entropy ceramic powders, yet their scalable production for industrial applications is lacking. In this work, for the first time, a densified microzone molten salt (DMMS) approach was developed for the scale-up preparation of high-entropy ceramic powders, including zirconates, hafnates, silicates, and carbides. The "densified" block of DMMS permitted only trace evaporation of molten salt on surfaces, and the internal "microzone" salt pools significantly promoted the *in situ* formation of high-entropy phases at relatively low temperatures. Single-phase $(La_{0.2}Nd_{0.2}Sm_{0.2}Eu_{0.2}Gd_{0.2})_2Zr_2O_7$ (HEZO) powders, as an example, could be synthesized with only ~10 wt% volatilization of NaCl–KCl–NaF salt during 1200 °C treatment, while the resulting powders prepared by the traditional powdery method contained segregation phases with a salt loss as high as ~95 wt%. By simply accommodating the "densified" blocks in a tunnel kiln, scale-up synthesis of high-entropy ceramic powders by DMMS can be realized for industrial production.

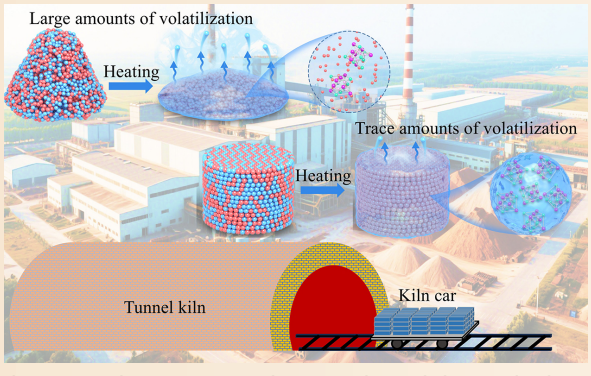

KEYWORDS: high-entropy ceramic powders; microzone molten salt; zirconate; scale-up synthesis

1 Introduction

Over the past decade, high-entropy materials have emerged as a prominent research focus due to their four core effects, the unique characteristics of which have substantially expanded their property space and application potential [1–6]. A growing number of high-entropy materials have been developed, including oxides [7–13], borides [14–16], carbides [17], nitrides [18], sulfides [19], and silicides [20], which have promising applications in the fields of thermal protection, energy storage, catalysis, and superconductivity [21,22]. The development of a low-cost route for the scale-up synthesis of high-entropy ceramic powders is of great importance to enable their widespread application.

Currently, the predominant methods for synthesizing high-entropy ceramic powders include high-temperature solid-state reactions and coprecipitation techniques [23–33]. For instance, Zhao *et al.* [34] synthesized $(La_{0.2}Ce_{0.2}Nd_{0.2}Sm_{0.2}Eu_{0.2})_2Zr_2O_7$ powders via a coprecipitation method at 1500 °C for 1 h. Hutterer and Lepple [35] reported the synthesis of $(Dy_{0.2}Nd_{0.2}Sm_{0.2}Er_{0.2}Gd_{0.2})_2Zr_2O_7$ powders using a reverse coprecipitation method at 1500 °C for 10 h. Teng *et al.* [36] and Li *et al.* [37] synthesized $(La_{0.2}Ce_{0.2}Nd_{0.2}Sm_{0.2}Eu_{0.2})_2Zr_2O_7$ powders at 1500 °C for 40 and 3 h, respectively, via a solid-state reaction. As recently reported, the kinetic effect plays a pivotal role in the formation of rare-earth-based high-entropy oxides, where sluggish cationic diffusion often hinders the homogenization process [38]. Consequently, these conventional techniques typically require prolonged exposure to high temperatures to overcome kinetic barriers, which implies high energy consumption and phase segregation during the cooling process. Thus, the efficient synthesis of high-entropy ceramic powders remains a critical challenge.

Molten salt synthesis [4,39–45] is a well-established chemical method for powder preparation. Reactants dissolve and diffuse within a liquid medium, effectively addressing the issue of long diffusion paths found in solid-solid reactions, thus significantly lowering reaction temperatures and times [46]. The added salt medium can be fully removed through water washing, ensuring high product purity and recycling of metal salts [47–53]. Xue *et al.*

† Yongxin Wang and Ling Zhang contributed equally to this work.

[1] State Key Laboratory of Advanced Refractories, Wuhan University of Science and Technology, Wuhan 430081, China. [2] Joint International Research Laboratory of Refractories and Metallurgy, Wuhan University of Science and Technology, Wuhan 430081, China. [3] School of Energy and Power Engineering, Changsha University of Science & Technology, Changsha 410014, China. [4] College of Engineering, Mathematics and Physical Sciences, University of Exeter, Exeter EX4 4QF, UK.

✉ Corresponding authors. E-mail: Z. Huang, huangzhong@wust.edu.cn; J. Cao, caojinhui@hnu.edu.cn; S. Zhang, s.zhang@exeter.ac.uk

Received: November 25, 2025; Revised: March 1, 2026; Accepted: March 2, 2026

© The Author(s) 2026. This is an open access article under the terms of the Creative Commons Attribution 4.0 International License (CC BY 4.0, http://creativecommons.org/licenses/by/4.0/).

[27] reported the synthesis of phase-pure rock salt-type $(Mg_{0.2}Co_{0.2}Ni_{0.2}Cu_{0.2}Zn_{0.2})O$ using 500 wt% salt dosage. Wei *et al.* [54] achieved the synthesis of pure $(Er_{0.25}Tm_{0.25}Yb_{0.25}Lu_{0.25})_2Si_2O_7$ and $(Er_{0.25}Tm_{0.25}Yb_{0.25}Lu_{0.25})_2SiO_5$ powders at 900 and 800 °C, respectively, using a 10 : 1 mass ratio of KCl–LiCl to reactant. However, the traditional molten salt method still presents several challenges: (1) Molten salt exhibits volatility at elevated temperatures, necessitating excessive amounts to maintain the liquid-phase environment required for powder synthesis. This leads to substantial salt consumption, significantly increasing synthesis costs. (2) "Powdery" synthesis with a salt medium restricts the yield of powder products, posing challenges for mass production. (3) High-temperature volatilization of substantial salt quantities induces severe corrosion of production equipment, as illustrated in Fig. 1(a).

Thus, in this paper, we developed a densified microzone molten salt (DMMS) synthesis approach that is built upon the advantages of conventional molten salt (CMS) techniques, enabling efficient and scalable synthesis of high-entropy ceramic powders while significantly reducing both salt consumption and evaporation. In this approach, the salt and oxides were compressed into a dense block, promoting intimate contact between particles and accelerating solid-state reactions, which also limits salt volatilization, thereby minimizing corrosion of heating equipment and reducing environmental emissions during processing. Additionally, this method improves the salt recovery rate, further lowering production costs, as illustrated in Fig. 1(b). The block form is particularly suited for industrial production, as it allows direct stacking on kiln cars and firing in tunnel kilns without complex handling, as shown in Fig. 1(c). Using this technique, we successfully synthesized single-phase $(La_{0.2}Nd_{0.2}Sm_{0.2}Eu_{0.2}Gd_{0.2})_2Zr_2O_7$ (HEZO) powders with a pure pyrochlore structure and uniform elemental distribution on a large scale using rare-earth elements (La_2O_3, Nd_2O_3, Sm_2O_3, Eu_2O_3, and Gd_2O_3) and ZrO_2 as raw materials and a NaCl–KCl–NaF eutectic mixture as a molten salt medium. Finally, to demonstrate the broad applicability of the DMMS approach, a range of high-entropy oxides and nonoxide ceramic powders, including $(La_{1/6}Nd_{1/6}Sm_{1/6}Eu_{1/6}Gd_{1/6}Y_{1/6})_2Zr_2O_7$, $(La_{1/7}Nd_{1/7}Sm_{1/7}Eu_{1/7}Gd_{1/7}Y_{1/7}Ce_{1/7})_2Zr_2O_7$, $(La_{0.2}Nd_{0.2}Sm_{0.2}Eu_{0.2}Gd_{0.2})_2Hf_2O_7$, $(Er_{0.2}Tm_{0.2}Yb_{0.2}Lu_{0.2}Y_{0.2})_2Si_2O_7$, and $(Ta_{0.25}Nb_{0.25}Ti_{0.25}V_{0.25})C$ powders, were also synthesized. These results confirm the applicability and scalability of current DMMS for the scale-up synthesis of a wide variety of high-entropy ceramic powders.

2 Experimental

2.1 Fabrication of HEZO powders

Oxides (La_2O_3, Nd_2O_3, Sm_2O_3, Eu_2O_3, Gd_2O_3, Y_2O_3, Er_2O_3, Ta_2O_3, Lu_2O_3, Yb_2O_3, Tm_2O_3, Ce_2O_3, Ta_2O_3, Nb_2O_3 ZrO_2, HfO_2, VO_2, TiO_2, and SiO_2, 99.9% purity, Aladdin Biochemical Technology Co., Ltd., China) were used without any treatment. KCl, NaCl, NaF, and $CaCl_2$ were purchased from Sinopharm Chemical Reagent Co., Ltd., China. All the chemical reagents used in this work were of analytical grade.

HEZO powders were synthesized using rare earth oxide (La_2O_3, Nd_2O_3, Sm_2O_3, Eu_2O_3, and Gd_2O_3) and ZrO_2 as raw materials and NaCl–KCl–NaF (the specific molar ratio is 0.58 : 0.32 : 0.10) as the reaction medium, which was prepared using DMMS, as shown in Fig. 2. First, the mixtures of the raw material powders with stoichiometric ratios were ball-milled (speed of 400 r/min) with zirconia spheres and ethanol in a planetary ball mill (QM-3SP2, Nanjing Nanda Co., Ltd., China) to obtain a slurry with fully mixed oxides [55]. The slurry was dried in an oven, ground, and sieved. Afterwards, a certain amount of powders was weighed and statically pressed under a pressure tester at 200 MPa for 3 min to make block samples with different sizes (ϕ20 mm, ϕ36 mm, ϕ50 mm, and 25 mm × 25 mm × 140 mm). These block samples were first heated to 1000 °C at a heating rate of 5 °C/min and then to 1200 °C at a heating rate of 4 °C/min and held at 1200 °C for 1–3 h. After that, these fired blocks were washed repeatedly with distilled water, which would disintegrate into a powdery case after removing the residual salts. Finally, the as-obtained powders were dried at 80 °C for further characterization. Other high-entropy ceramic powders, including zirconates, hafnates, silicates, and carbide, were also prepared, and their preparation parameters are listed in Table S1 in the Electronic Supplementary Material (ESM).

2.2 Characterizations

The crystal structures of the samples were measured by a powder X-ray diffractometer (XRD; X' pert pro, Philips, the Netherlands) at 40 kV and 40 mA using Cu Kα radiation (λ = 0.1542 nm). ICDD cards (Nos. 75-0346, 73-0444, 24-0410, 24-0999, 24-0425, 24-0778, 37-1040, 43-1021, 65-8786, and 65-8796) were used for the identification of $(LaSm)_2Zr_2O_7$, $La_2Zr_2O_7$, $Eu_2Hf_2O_7$, $Gd_2Hf_2O_7$, $Nd_2Hf_2O_7$, $Sm_2Hf_2O_7$, $La_2Hf_2O_7$, $RE_2Si_2O_7$, $NbTiC_2$,

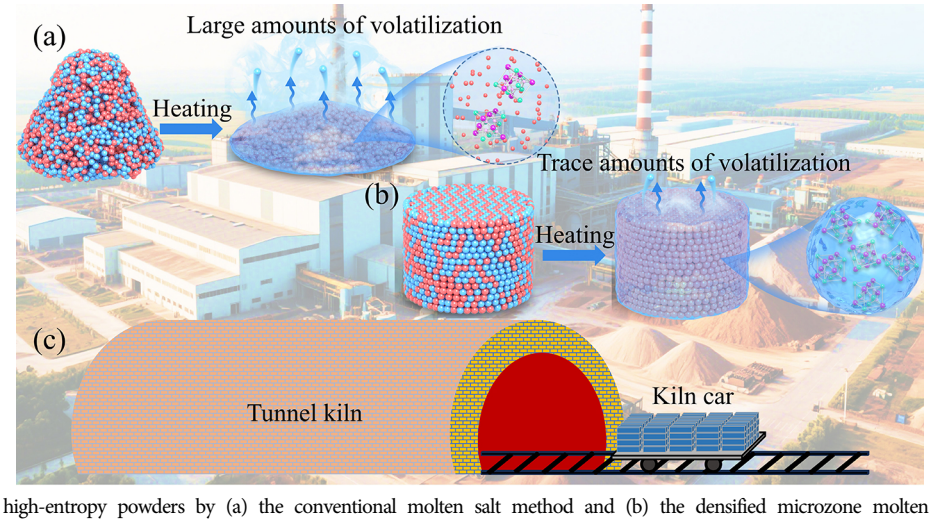

Fig. 1 Preparation of high-entropy powders by (a) the conventional molten salt method and (b) the densified microzone molten salt (DMMS) method, and (c) schematic illustration of ton-scale production using a tunnel kiln.

and $TiTaC_2$, respectively. A laser particle size analyzer (LPSA; Mastersizer 2000, MALVERN, UK) was used to determine the particle size range of the samples. A field emission scanning electron microscope (FE-SEM; Nova 400 Nano, FEI, USA) and a high-resolution transmission electron microscope (HRTEM; JEM-2100UHRS, JEOL, Japan) were used to observe the microstructure of the samples. The chemical composition of the samples was analyzed by an X-ray energy dispersive spectroscope (EDS; JEOL, Japan). The chemical bonding state of the samples was examined with an X-ray photoelectron spectroscope (XPS; VG Multilab 2000, Thermo Fisher, USA).

3 Results and discussion

3.1 DMMS synthesis of HEZO powders

Figure 3(a) shows the XRD patterns of HEZO powders (DMMS) prepared at temperatures ranging from 1000 to 1200 °C for 3 h.

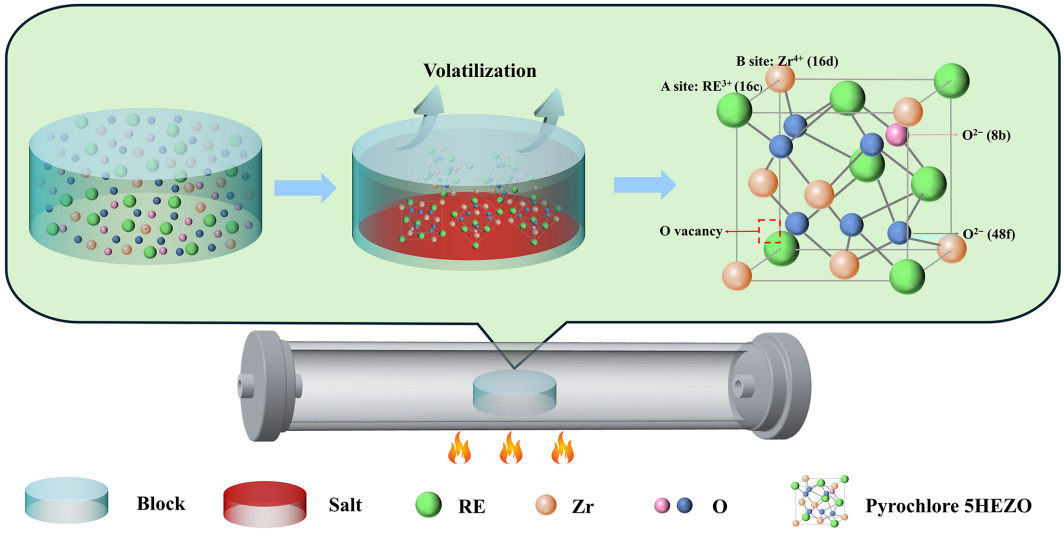

Fig. 2 Schematic diagram of the preparation process of HEZO powders by DMMS.

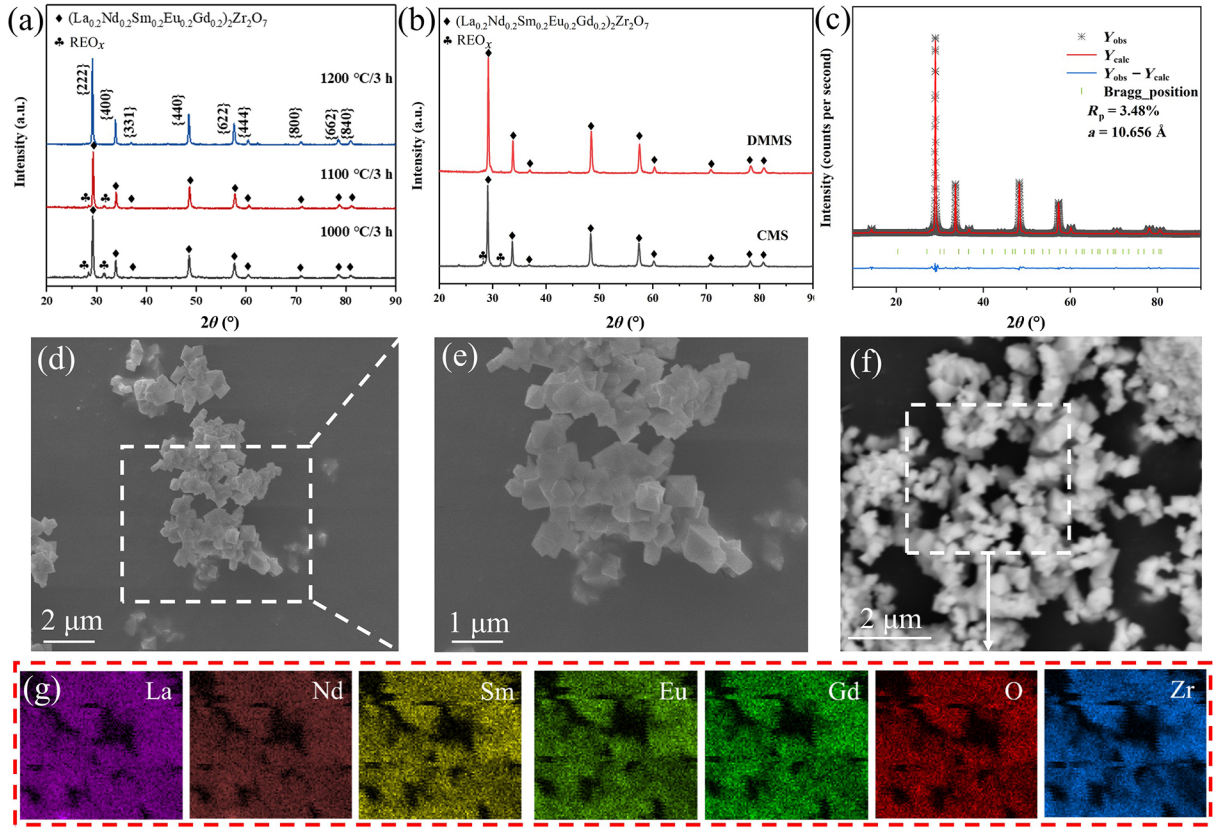

Fig. 3 (a) XRD patterns of as-synthesized samples at different temperatures prepared by DMMS. (b) XRD patterns of samples synthesized by the DMMS and CMS methods. (c) Rietveld refinement pattern and (d–f) SEM images of as-synthesized HEZO powders prepared by DMMS. (g) EDS mapping results of the region marked by the white box in (f).

清華大学出版社 Tsinghua University Press | SciOpen

The sample calcined at 1000 °C contained both rare earth oxides (REO_x) and HEZO phase. As the temperature increased, the REO_x diffraction peaks decreased and disappeared entirely at 1200 °C, resulting in a pure pyrochlore-type HEZO phase [56–58]. The XRD patterns of the samples prepared by DMMS and CMS at 1200 °C are presented in Fig. 3(b). When the salt and oxides were uniformly mixed and then directly heat-treated, the REO_x phase still existed, while when the mixed powders were pressed into a block, the REO_x phase disappeared, and only the HEZO single phase was detected in the samples. Figure S1 in the ESM displays the XRD patterns of HEZO calcined at 1200 °C for different holding times. After 1 h of calcination, the Gd_2O_3 and ZrO_2 phases coexisted with the HEZO phase. When the holding time was extended to 2 and 3 h, the Gd_2O_3 and ZrO_2 phases disappeared, leaving only the pure HEZO phase. The phase composition of the sample synthesized at 1200 °C for 2 h was further analyzed by the Rietveld method (Fig. 3(c)), which revealed a phase-pure pyrochlore-type structure (space group: $Fd\bar{3}m$; lattice parameter: 10.656 Å). The crystal structure of HEZO depends on the radius ratio of the cations (R_{RE}/R_{Zr}). It exhibited a pyrochlore-type structure when $1.46 < R_{RE}/R_{Zr} < 1.78$ and a defective-type fluorite structure when $R_{RE}/R_{Zr} < 1.46$ [59]. In the current work, the calculated R_{RE}/R_{Zr} of $(La_{0.2}Nd_{0.2}Sm_{0.2}Eu_{0.2}Gd_{0.2})_2Zr_2O_7$ was 1.52, which corresponded to the pyrochlore-type structure and was consistent with the XRD results. Based on these results, it could be concluded that phase-pure HEZO powders can be successfully synthesized by using the DMMS method.

The SEM images of as-prepared powders are shown in Figs. 3(d) and 3(e). The HEZO powders exhibited a polyhedral morphology with numerous octahedral shapes of the pyrochlore phase, and the grain size ranged from approximately 0.2 to 0.5 μm. Furthermore, the EDS elemental mapping results (Figs. 3(f) and 3(g)) revealed that rare earth (RE), zirconium, and oxygen were uniformly distributed throughout the entire field, indicating that all samples were chemically homogeneous. The particle size distribution of the final HEZO powders was analyzed in Fig. S2 in the ESM, which exhibited a narrow and unimodal distribution with a Brunauer–Emmett–Teller (BET) specific surface area of 2.273 m^2/g, indicating the uniform particle growth without severe agglomeration. Additionally, the elemental composition and chemical state of the samples were analyzed using XPS (Figs. S3 and S4 in the ESM), which further indicated that the HEZO powders were successfully prepared.

The microstructure, phase composition, and mechanical properties of ceramics prepared from HEZO and $La_2Zr_2O_7$ (LZ) powders were systematically investigated, as shown in Fig. S5 in the ESM. The prepared LZ ceramics had a Vickers hardness of 5.29±2.48 GPa (Fig. S5(d) in the ESM), a nanohardness of 7.75±1.12 GPa, and a Young's modulus of 164.06±10.14 GPa (Fig. S5(g) in the ESM). In contrast, the HEZO ceramics exhibited a higher Vickers hardness (14.29±0.48 GPa) (Fig. S5(d) in the ESM) and nanohardness (15.74±0.45 GPa) and a larger Young's modulus (200.33±8.50 GPa) (Fig. S5(g) in the ESM). The coefficient of friction (COF) and wear rates (Figs. S5(h) and S5(i) in the ESM) of the HEZO ceramics (0.005 and 3.10×10^{-12} $m^3/(N\cdot m)$) were smaller than those of the LZ ceramics (0.046 and 5.80×10^{-12} $m^3/(N\cdot m)$), indicating that the HEZO ceramics had better mechanical stability and wear resistance. In addition, the corrosion resistance to CaO–MgO–Al_2O_3–SiO_2 (CMAS) slag of HEZO and LZ ceramics was also investigated (Table S2 and Figs. S6 and S7 in the ESM), showing that the former ceramics exhibited better corrosion resistance, including a lower infiltration rate and slower corrosion time.

3.2 Large-scale production of DMMS

To assess the scalable production of HEZO powders using the DMMS method, the influence of densified block sizes (ϕ20 mm, ϕ36 mm, ϕ50 mm, and 25 mm × 25 mm × 140 mm; Fig. 4(a)) on HEZO synthesis was investigated. As shown in Figs. 4(a) and 4(b), all samples retained their original shape with minor shrinkage after calcination. The salt volatilization rate, calculated by comparing the sample weights before and after calcination, was significantly lower in the case of DMMS (10–20 wt%) than in the CMS method (~95 wt%) (Fig. 4(c)). More importantly, the yield of HEZO powders increased proportionally with densified block size, ranging from 2.66 g (ϕ20 mm) to 71.53 g (25 mm × 25 mm × 140 mm), which were all in close agreement with the theoretical yields. Notably, the low and stable salt volatilization rate (Fig. 4(c)) helped to minimize the corrosion of the furnace and facilitate the recovery of the washing salts. The XRD analysis confirmed that all powders exhibited a single-phase pyrochlore structure with no detectable impurities (Fig. 4(d)). These results indicated that increasing the sample size did not affect the phase purity but significantly enhanced the product yield. It was reasonable to expect that even with further scale-up, the phase purity and low salt volatility would be maintained with a reduced overall production cost.

Since lab-scale preparation is limited by the chamber size of the muffle furnace, our DMMS method is well suited for industrial-scale production using tunnel kilns, as illustrated in Fig. 1(c). A typical medium-sized tunnel kiln has internal dimensions of 100–150 m in length, 1.8–3.6 m in width, and 2.6 m in height. The kiln cars commonly used in such systems have dimensions of approximately length (1.0–1.5 m) × width (1.0–1.5 m) × height (0.6–0.9 m). Taking a representative block with a size of 25 mm × 25 mm × 140 mm, a single kiln car can accommodate approximately 8820 blocks, and the total mass loaded on one kiln car is ~2205 kg. Based on the laboratory-scale yield, the corresponding output of HEZO powders will be 1102.5 kg. Considering the continuous production process of tunnel kilns, it will be very easy to achieve a ton-level production. Based on these results, DMMS allows for direct, large-volume processing without any specialized equipment, and its low salt volatility, ton-level production mode, and compatibility with industrial kilns make it a promising approach for efficient and scalable production of high-entropy ceramic powders.

3.3 Synthesis mechanism of DMMS

Figures 5(a) and 5(b) show the appearances of the densified blocks with varying salt contents before and after 1200 °C calcination, respectively. The samples without salt and with 1 : 1 (mass ratio, salt relative to the reactants) remained essentially unchanged in shape after calcination. The former exhibited a slight expansion, while the latter showed minor shrinkage. In contrast, the block samples with 3 : 1 and 5 : 1 were melted completely, forming a salt pool to promote the long-range diffusion between reactant species, which was similar to that of CMS using a powdery body. As a result, the recrystallized molten salt adhered to the surface of the crucible, which not only corroded the container but also made it difficult to recycle the molten salt.

The XRD patterns of the corresponding samples (Fig. 5(b)) are shown in Fig. S8 in the ESM. In the absence of salt, the diffraction peaks were broad, and REO_x and ZrO_2 peaks were present, suggesting that a salt medium was key to the low-temperature synthesis of HEZO. When the mass ratio of salt to reactant was 1 : 1, only the pyrochlore-type HEZO phase was detected. Unexpectedly, an excess of salt did not promote the yield of

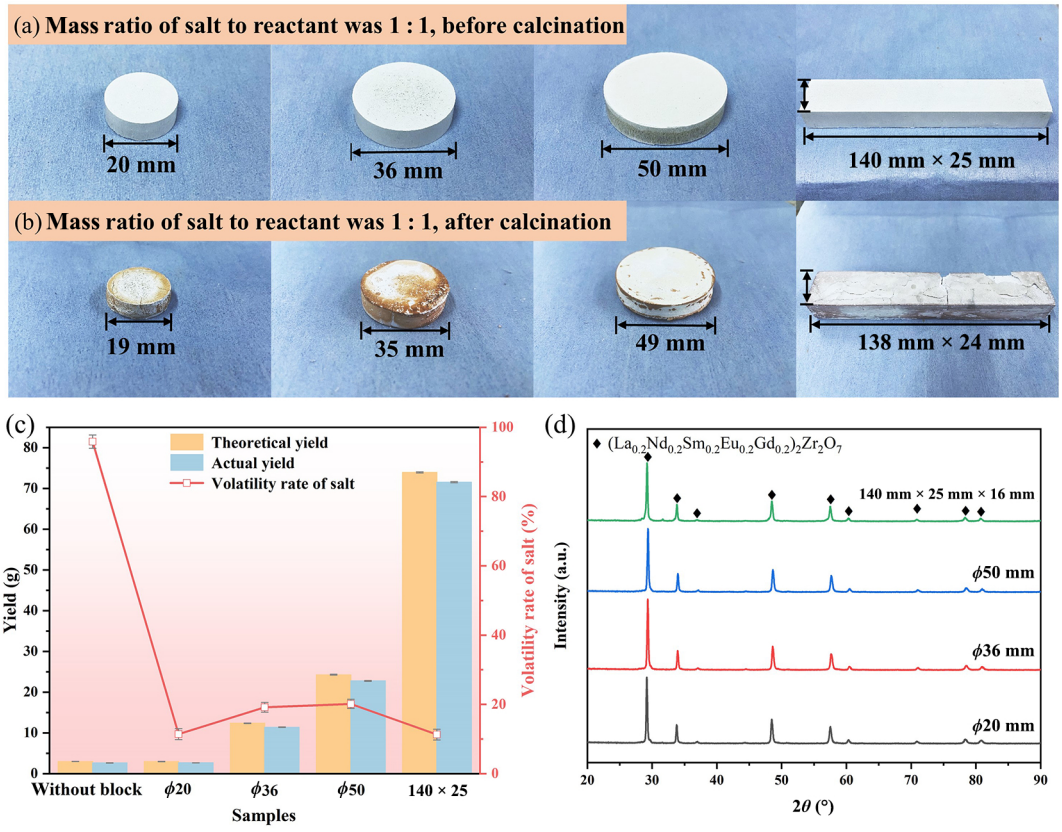

Fig. 4 (a, b) Photographs of densified blocks with different sizes before and after calcination. (c) Yields and salt volatilization rates of HEZO for different densified block sizes. (d) XRD patterns of as-synthesized samples with different densified block sizes.

HEZO; in contrast, impurity phases such as ZrO_2 appeared when the mass ratio of salt to reactant was greater than 3 : 1, which was a very unusual phenomenon in molten salt synthesis. As shown in Fig. S9 in the ESM, the salt volatilization rate decreased significantly with lower salt content, from 91.1 wt% in the 5 : 1 case to just 11.4 wt% in the 1 : 1 case. Figures 5(c) and 5(d) summarize the salt dosage and calcination conditions of HEZO synthesis using molten salt methods. In comparison, our work with only 1 : 1 salt and 1200 °C calcination significantly reduces both salt consumption and heating temperature [60–63], and the DMMS developed here enables an efficient synthesis of high-entropy ceramic powders.

Based on the above discussions, a "densified microzone" architecture could be proposed, in which the "densified" refers to the macroscopic sintering behavior of the block, while the "microzone" refers to the localized molten pools inside the block. As evidenced by the measurements in Fig. S10 in the ESM, the block underwent a significant densification process, with the porosity dropping from 31.29% to 20.84%. This shrinkage would create a strong physical confinement effect, which effectively reduced the diffusion channels for salt vapor [64]. Simultaneously, the internal microzone molten pools acted as a "reactor" (as indicated in Figs. S11 and S12 in the ESM) to facilitate the rapid dissolution and diffusion of reactants, ensuring a uniform elemental distribution and rapid reaction. From these, a plausible mechanism for DMMS preparation of HEZO is illustrated in Fig. 5(e). A densified block containing both reactants and salts is pressed, in which a uniform distribution of salt (KCl, NaCl, and NaF) around oxide particles (La_2O_3, Nd_2O_3, ZrO_2, etc.) ensures the interaction between them (I, Fig. 5(e)). During calcination, the integrity of the densified blocks in the 1 : 1 case could be maintained (Fig. 4(b)), and only a small portion of molten salt evaporated from the block surface during the whole DMMS process. As the temperature reaches the molten point of KCl–NaCl–NaF (548 °C), numerous "microzone" melt pools could be formed throughout the interior block (II, Fig. 5(e)), which provides a liquid reaction medium similar to the case of widely used CMS, facilitating the rapid formation of the HEZO phase at 1200 °C (III, Fig. 5(e)). In contrast to the case of salt-excess samples, the blocks undergo expansion, melting, or collapse from a macroscopic view (Fig. 5(b)), and even if there should be enough salt medium in the beginning, the molten salt evaporates violently during heating and holding periods (Fig. 5(c)), which accidentally leads to an incomplete reaction due to insufficient salt medium. Overall, the key to DMMS is to build the "densified microzone", in which the "densified" zone only allows for a trace amount of salt evaporation on the block surface, while the inside "microzone" salt pools support an *in situ* complete formation of HEZO at relatively low temperature.

3.4 Feasibility of DMMS

To verify the applicability of DMMS to other high-entropy ceramic powders, high-entropy zirconates with more components ($(La_{1/6}Nd_{1/6}Sm_{1/6}Eu_{1/6}Gd_{1/6}Y_{1/6})_2Zr_2O_7$ (Fig. 6(a)), $(La_{1/7}Nd_{1/7}Sm_{1/7}Eu_{1/7}Gd_{1/7}Y_{1/7}Ce_{1/7})_2Zr_2O_7$) (Fig. 6(b)), hafniate ($(La_{0.2}Nd_{0.2}Sm_{0.2}Eu_{0.2}Gd_{0.2})_2Hf_2O_7$) (Fig. S13(a)), silicate ($(Er_{0.2}Tm_{0.2}Yb_{0.2}Lu_{0.2}Y_{0.2})_2Si_2O_7$) (Fig. S13(b) in the ESM), and carbide ($(Ta_{0.25}Nb_{0.25}Ti_{0.25}V_{0.25})C$) (Fig. S14 in the ESM) were prepared by DMMS. XRD and SEM analyses confirmed that all these samples were single-phase. For example, as shown in Figs. 6(c) and 6(d), $(La_{1/6}Nd_{1/6}Sm_{1/6}Eu_{1/6}Gd_{1/6}Y_{1/6})_2Zr_2O_7$ exhibited irregular granules, and some particles aggregated into large clusters. The corresponding EDS elemental mapping (Fig. 6(e)) revealed a homogeneous distribution of all eight constituent elements. To

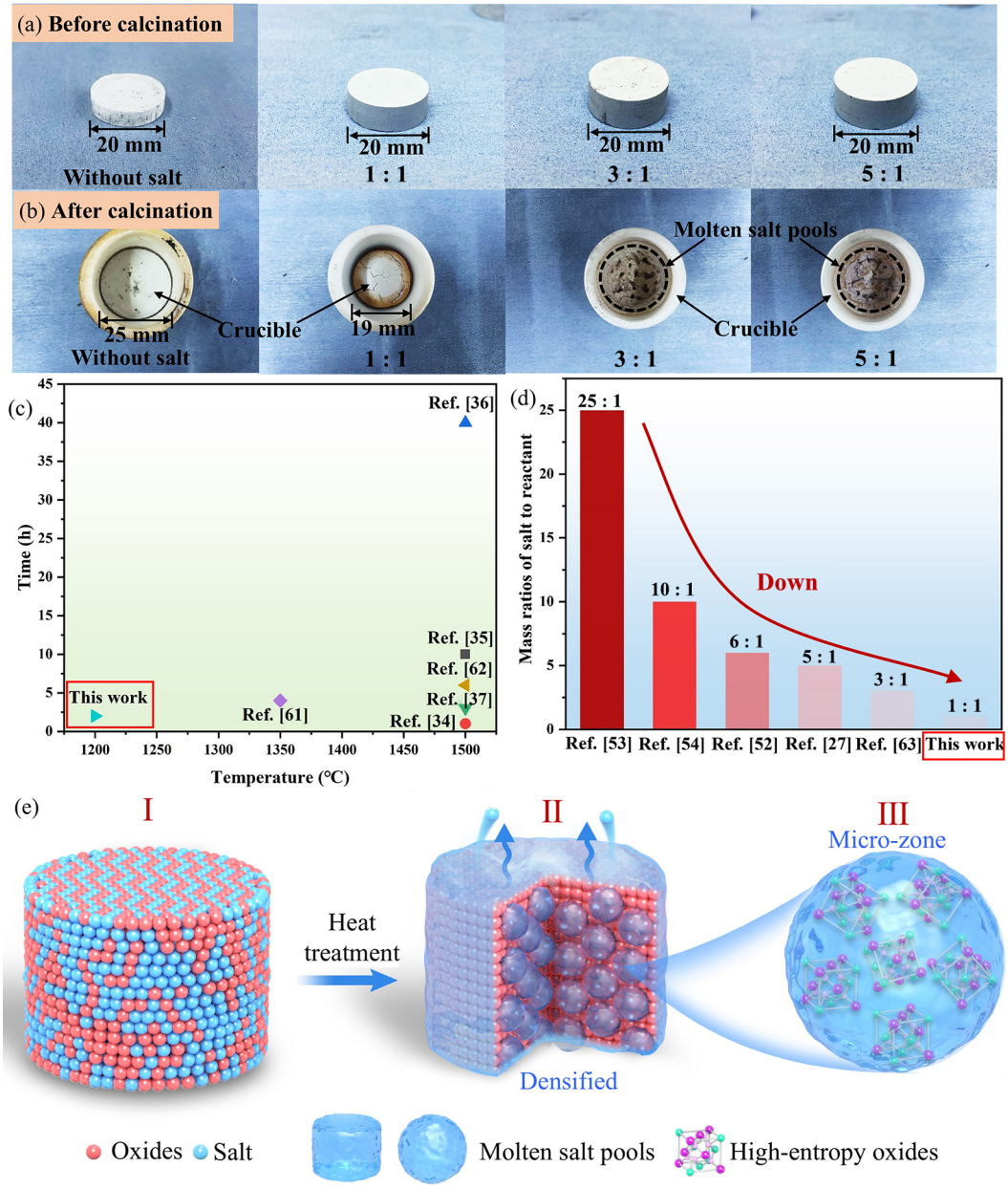

Fig. 5 (a, b) Photographs showing the appearances of densified blocks with different mass ratios of salt to reactant before and after calcination. (c) Comparison of experimental conditions required for the synthesis of pure HEZO phases. (d) Comparison of the mass ratio of salt to reactant with the works reported previously, and (e) Schematic illustration of the densified microzone during DMMS preparation of HEZO.

further investigate the elemental distribution and structural characteristics, TEM and HRTEM analyses were conducted. Figure 6(f) shows that the grain size of these irregular particles was on the order of hundreds of nanometers. The HRTEM image in Fig. 6(g) displays a lattice spacing of 0.301 nm, corresponding to the (111) plane of the yttrium zirconate-type structure $(LaSm)_2Zr_2O_7$ (JCPDS No. 75-0346) [65,66]. Elemental mapping at the nanoscale (Fig. 6(h)) also verified a uniform distribution of La, Nd, Sm, Gd, Yb, Zr, and O. Similar structural and compositional homogeneity was observed in the other high-entropy ceramic powders in Figs. S15–S19 in the ESM.

4 Conclusions

In summary, we demonstrated, for the first time, a scale-up DMMS strategy for the mass production of high-entropy zirconates, hafniates, silicates, and carbides that fundamentally resolves the trade-off between synthesis efficiency and salt volatility in the molten salt method. By confining a compacted reactant matrix, the internal "microzone" salt pools facilitate rapid mass transfer and phase formation at relatively low temperatures (1200 °C), while the "densified" block significantly suppresses salt volatilization with a minimal 1 : 1 salt-to-reactant ratio. The as-developed DMMS could be considered an ideal method to prepare ceramic powders based on 1) the limited salt volatilization, not only minimizing salt corrosion of high-temperature equipment but also ensuring the reuse of molten salt after washing; 2) a low dosage of molten salt, reducing preparation costs; 3) the applicability to various high-entropy ceramic powders; and 4) the potential for industrial production, which could achieve the large-scale production relying only on traditional kilns or atmosphere-controlled sintering furnaces.

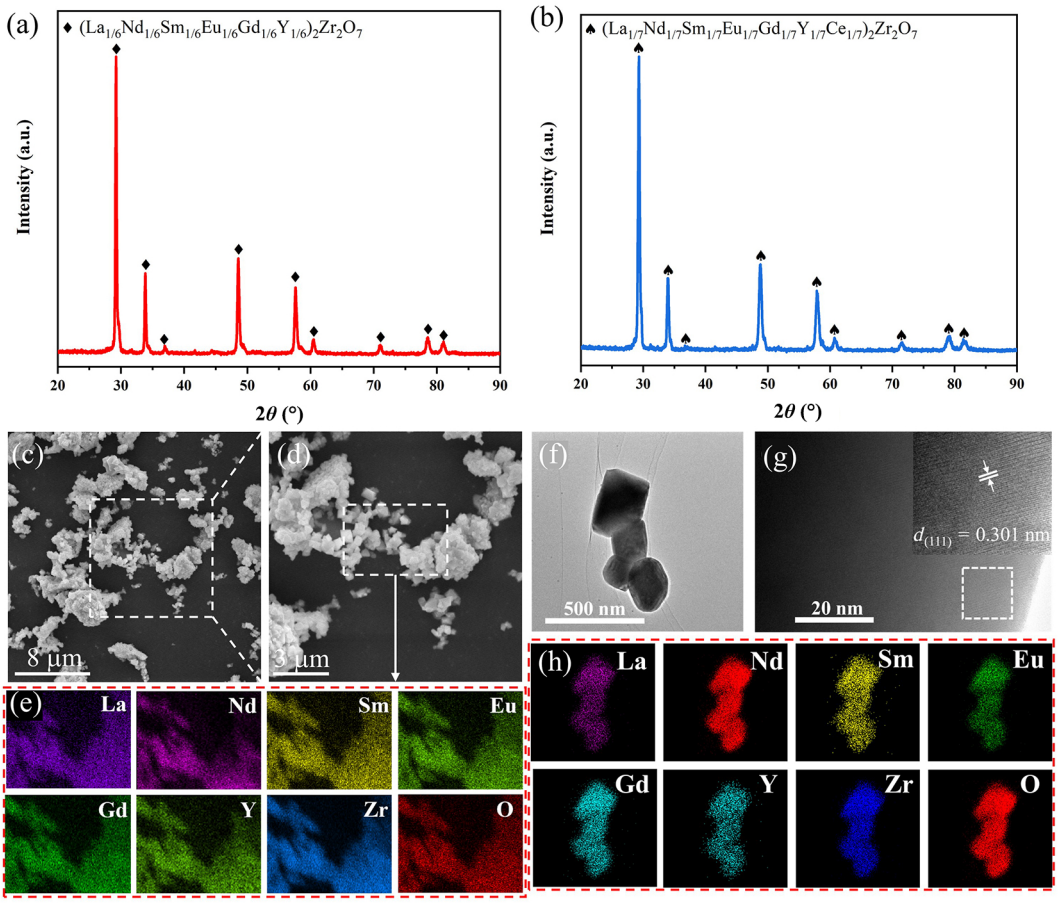

Fig. 6 XRD patterns of as-synthesized (a) $(La_{1/6}Nd_{1/6}Sm_{1/6}Eu_{1/6}Gd_{1/6}Y_{1/6})_2Zr_2O_7$ and (b) $(La_{1/7}Nd_{1/7}Sm_{1/7}Eu_{1/7}Gd_{1/7}Y_{1/7}Ce_{1/7})_2Zr_2O_7$ powders. (c, d) SEM images, (e) elemental mapping results, (f) TEM image, (g) HRTEM image, and (h) TEM-EDS elemental mappings of $(La_{1/6}Nd_{1/6}Sm_{1/6}Eu_{1/6}Gd_{1/6}Y_{1/6})_2Zr_2O_7$ powders.

Acknowledgements

This work was financially supported by the National Natural Science Foundation of China (Nos. U23A20559, 52202025, and 52304319), the Wuhan Metropolitan Area Collaborative Innovation Technology Project (No. 2025070604020038), the Hunan Province "Huxiang Talents" Project (No. 2024RC3164), and "The 14th Five-Year Plan" Hubei Provincial Advantaged Characteristic Disciplines (Groups) Project of Wuhan University of Science and Technology (No. 2023A0307).

Availability of data and materials

The data that support the findings of this study are available from the corresponding author upon reasonable request.

Competing interests

The authors have no competing interests to declare that are relevant to the content of this article.

Electronic Supplementary Material

Supplementary material is available in the online version of this article at https://doi.org/10.26599/JAC.2026.9221273.

References

[1] Hsu WL, Tsai CW, Yeh AC, *et al.* Clarifying the four core effects of high-entropy materials. *Nat Rev Chem* 2024, **8**: 471–485.

[2] Divilov S, Eckert H, Hicks D, *et al.* Disordered enthalpy–entropy descriptor for high-entropy ceramics discovery. *Nature* 2024, **625**: 66–73.

[3] Yuan MJ, Guo XT, Liu Y, *et al.* Si-based materials derived from biomass: Synthesis and applications in electrochemical energy storage. *J Mater Chem A* 2019, **7**: 22123–22147.

[4] Li ZY, Li KZ, Li YG, *et al.* Modified molten salt assisted exfoliation of large-size 2D materials. *Adv Funct Mater* 2024, **34**: 2310371.

[5] Liu XF, Li XK, Li YG, *et al.* High-entropy oxide: A future anode contender for lithium-ion battery. *EcoMat* 2022, **4**: 12261.

[6] Wang Q, Hu Q, Wang HL, *et al.* Investigations on the microstructures and tribological behaviors of as-cast $CrFeCoNiCu_x$ high entropy alloys. *Intermetallics* 2023, **157**: 107886.

[7] Fracchia M, Coduri M, Ghigna P, *et al.* Phase stability of high entropy oxides: A critical review. *J Eur Ceram Soc* 2024, **44**: 585–594.

[8] Aamlid SS, Oudah M, Rottler J, *et al.* Understanding the role of entropy in high entropy oxides. *J Am Chem Soc* 2023, **145**: 5991–6006.

[9] Li LL, Ji PC, Geng C, *et al.* Facile synthesis of high-entropy $(Co_{0.2}Cr_{0.2}Fe_{0.2}Mn_{0.2}Ni_{0.2})_3O_4$ nanopowders and their electrochemical properties as supercapacitor electrode. *J Energy Storage* 2023, **73**: 109182.

[10] Liu XF, Xing YY, Xu K, *et al.* Kinetically accelerated lithium storage in high-entropy (LiMgCoNiCuZn)O enabled by oxygen vacancies. *Small* 2022, **18**: 2200524.

[11] Liu XF, Yu YJ, Li KZ, *et al.* Intergrating hollow multishelled structure and high entropy engineering toward enhanced mechano-electrochemical properties in lithium battery. *Adv Mater* 2024, **36**: 2312583.

[12] Sun XY, Zeng XH, He X, *et al.* Influence of oxygen vacancies on the structure and magnetic properties of high entropy $(Co,Cr,Fe,Mn,Ni)_3O_4$ ceramics. *J Alloys Comp* 2022, **925**: 166560.

[13] Karabaş M. Production and characterization of Nd and Dy doped

lanthanum zirconate-based thermal barrier coatings. *Surf Coat Tech* 2020, **394**: 125864.
[14] Smith SM, Fahrenholtz WG, Hilmas GE. Pressureless sintering of high-entropy boride ceramics. *J Eur Ceram Soc* 2023, **43**: 5168–5173.
[15] Qiao LJ, Liu Y, Gao Y, *et al.* First-principles prediction, fabrication and characterization of $(Hf_{0.2}Nb_{0.2}Ta_{0.2}Ti_{0.2}Zr_{0.2})B_2$ high-entropy borides. *Ceram Int* 2022, **48**: 17234–17245.
[16] Liu J, Yang QQ, Zou J, *et al.* Strong high-entropy diboride ceramics with oxide impurities at 1800 °C. *Sci China Mater* 2023, **66**: 2061–2070.
[17] Hu JJ, Yang QK, Zhu SY, *et al.* Superhard bulk high-entropy carbides with enhanced toughness *via* metastable *in-situ* particles. *Nat Commun* 2023, **14**: 5717.
[18] Nayak GK, Kretschmer A, Mayrhofer PH, *et al.* On correlations between local chemistry, distortions and kinetics in high entropy nitrides: An *ab initio* study. *Acta Mater* 2023, **255**: 118951.
[19] Lin L, Wang K, Sarkar A, *et al.* High-entropy sulfides as electrode materials for Li-ion batteries. *Adv Energy Mater* 2022, **12**: 2103090.
[20] Sharma P, Balasubramanian G. High configurational entropy driven increased heat capacity of refractory multicomponent di-silicides. *Materialia* 2023, **30**: 101861.
[21] Zeng LY, Wang ZQ, Song J, *et al.* Discovery of the high-entropy carbide ceramic topological superconductor candidate $(Ti_{0.2}Zr_{0.2}Nb_{0.2}Hf_{0.2}Ta_{0.2})C$. *Adv Funct Mater* 2023, **33**: 2301929.
[22] Zeng LY, Hu XW, Zhou YZ, *et al.* Superconductivity in the high-entropy ceramics $Ti_{0.2}Zr_{0.2}Nb_{0.2}Mo_{0.2}Ta_{0.2}C_x$ with possible nontrivial band topology. *Adv Sci* 2024, **11**: 2305054.
[23] Tomboc GM, Zhang XD, Choi S, *et al.* Stabilization, characterization, and electrochemical applications of high-entropy oxides: Critical assessment of crystal phase–properties relationship. *Adv Funct Mater* 2022, **32**: 2205142.
[24] Akrami S, Edalati P, Fuji M, *et al.* High-entropy ceramics: Review of principles, production and applications. *Mat Sci Eng R* 2021, **146**: 100644.
[25] Witte R, Sarkar A, Kruk R, *et al.* High-entropy oxides: An emerging prospect for magnetic rare-earth transition metal perovskites. *Phys Rev Materials* 2019, **3**: 034406.
[26] Wright AJ, Huang CY, Walock MJ, *et al.* Sand corrosion, thermal expansion, and ablation of medium- and high-entropy compositionally complex fluorite oxides. *J Am Ceram Soc* 2021, **104**: 448–462.
[27] Xue TY, Liu XF, Lei HC, *et al.* One-step molten salt synthesis of high entropy oxides. *Ceram Int* 2024, **50**: 18294–18302.
[28] Han Y, Liu XY, Zhang QQ, *et al.* Ultra-dense dislocations stabilized in high entropy oxide ceramics. *Nat Commun* 2022, **13**: 2871.
[29] Xu L, Su L, Wang HJ, *et al.* High-entropy $Sm_2B_2O_7$ (B = Ti, Zr, Sn, Hf, Y, Yb, Nb, and Ta) oxides with highly disordered B-site cations for ultralow thermal conductivity. *J Mater Sci Technol* 2022, **119**: 182–189.
[30] Cheng FH, Zhang FN, Liu YF, *et al.* Ti^{4+}-incorporated fluorite-structured high-entropy oxide $(Ce,Hf,Y,Pr,Gd)O_{2-\delta}$: Optimizing preparation and CMAS corrosion behavior. *J Adv Ceram* 2022, **11**: 1801–1814.
[31] Oses C, Toher C, Curtarolo S. High-entropy ceramics. *Nat Rev Mater* 2020, **5**: 295–309.
[32] Liu ZY, Liu Y, Xu YJ, *et al.* Novel high-entropy oxides for energy storage and conversion: From fundamentals to practical applications. *Green Energy Environ* 2023, **8**: 1341–1357.
[33] Ma SH, Wang QH, Li YW, *et al.* Novel $(La_{0.2}Eu_{0.2}Nd_{0.2}Sm_{0.2}Pr_{0.2})(Al_{0.6}Co_{0.4})O_{3-\delta}$ and $(La_{0.2}Eu_{0.2}Nd_{0.2}Sm_{0.2}Ca_{0.2})(Al_{0.6}Co_{0.4})O_{3-\delta}$ high-entropy ceramics with high emissivity and low degradation. *Ceram Int* 2024, **50**: 13366–13377.
[34] Zhao ZF, Xiang HM, Dai FZ, *et al.* $(La_{0.2}Ce_{0.2}Nd_{0.2}Sm_{0.2}Eu_{0.2})_2Zr_2O_7$: A novel high-entropy ceramic with low thermal conductivity and sluggish grain growth rate. *J Mater Sci Technol* 2019, **35**: 2647–2651.
[35] Hutterer P, Lepple M. Influence of composition on structural evolution of high-entropy zirconates–cationic radius ratio and atomic size difference. *J Am Ceram Soc* 2023, **106**: 1547–1560.
[36] Teng Z, Zhu LN, Tan YQ, *et al.* Synthesis and structures of high-entropy pyrochlore oxides. *J Eur Ceram Soc* 2020, **40**: 1639–1643.
[37] Li F, Zhou L, Liu JX, *et al.* High-entropy pyrochlores with low thermal conductivity for thermal barrier coating materials. *J Adv Ceram* 2019, **8**: 576–582.
[38] Spiridigliozzi L, Monfreda V, Marocco A, *et al.* On the effect of kinetics on the formation of fluorite/bixbyite-structured entropy-stabilized oxides. *Ceram Int* 2025, **51**: 30684–30692.
[39] Huang Z, Liu JH, Huang L, *et al.* One-step synthesis of dandelion-like lanthanum titanate nanostructures for enhanced photocatalytic performance. *NPG Asia Mater* 2020, **12**: 11.
[40] Huang Z, Li FL, Jiao CP, *et al.* Molten salt synthesis of $La_2Zr_2O_7$ ultrafine powders. *Ceram Int* 2016, **42**: 6221–6227.
[41] Huang Z, Liu JH, Deng XG, *et al.* Low temperature molten salt preparation of molybdenum nanoparticles. *Int J Refract Met H* 2016, **54**: 315–321.
[42] Liu JH, Huang Z, Huo CG, *et al.* Low-temperature rapid synthesis of rod-like ZrB_2 powders by molten-salt and microwave co-assisted carbothermal reduction. *J Am Ceram Soc* 2016, **99**: 2895–2898.
[43] Liang F, Tian L, Zhang HJ, *et al.* Low temperature synthesis of $LiSi_2N_3$ nanobelts via molten salt nitridation and their photoluminescence properties. *RSC Adv* 2016, **6**: 68615–68618.
[44] Ding J, Guo D, Deng CJ, *et al.* Low-temperature synthesis of nanocrystalline ZrC coatings on flake graphite by molten salts. *Appl Surf Sci* 2017, **407**: 315–321.
[45] Ding J, Zhu HX, Li GQ, *et al.* Catalyst-assisted synthesis of α-Si_3N_4 in molten salt. *Ceram Int* 2016, **42**: 2892–2898.
[46] Liu T, Ma BY, Zan WY, *et al.* Green preparation of high entropy ceramics $(Y_{0.2}Sm_{0.2}Eu_{0.2}Er_{0.2}Yb_{0.2})_2SiO_5$ with low thermal conductivity by molten salt synthesis. *Ceram Int* 2024, **50**: 2718–2726.
[47] Gupta SK, Mao YB. Recent developments on molten salt synthesis of inorganic nanomaterials: A review. *J Phys Chem C* 2021, **125**: 6508–6533.
[48] Liu XF, Feng G, Liu JM, *et al.* Effect of NaOH on the preparation of two-dimensional flake-like zirconia nanostructures. *Chem Phys Lett* 2020, **754**: 137755.
[49] Guan KK, Lei W, Wang HH, *et al.* Efficient synthesis of Ti_3AlC_2 powders with high purity by microwave-assisted molten salt method. *Ceram Int* 2022, **48**: 16357–16363.
[50] Gupta SK, Mao YB. A review on molten salt synthesis of metal oxide nanomaterials: Status, opportunity, and challenge. *Prog Mater Sci* 2021, **117**: 100734.
[51] Liu XF, Wang HH, Dong L, *et al.* Molten salt synthesis, morphology modulation, and lithiation mechanism of high entropy oxide for robust lithium storage. *J Energy Chem* 2023, **86**: 536–545.
[52] Liu JX, Yang H, Xue XX. Structure, morphology, and magnetic properties of $NiFe_2O_4$ powder prepared by molten salt method. *Powder Technol* 2019, **355**: 708–715.
[53] Hu ZM, Xiao X, Jin HY, *et al.* Rapid mass production of two-dimensional metal oxides and hydroxides via the molten salts method. *Nat Commun* 2017, **8**: 15630.
[54] Wei P, Zhuang L, Yu HL, *et al.* Low-temperature molten salt synthesis of ultrafine high-entropy rare-earth silicate powders. *J Am Ceram Soc* 2024, **107**: 1372–1382.
[55] Peng CZ, Huang WZ, Zhou X, *et al.* Microstructure and mechanical property regulation of plasma-sprayed high-entropy $(La_{0.2}Nd_{0.2}Sm_{0.2}Eu_{0.2}Gd_{0.2})_2Zr_2O_7$ thick coatings. *Ceram Int* 2024, **50**: 24781–24790.
[56] Xu JW, Xi R, Xu XL, *et al.* $A_2B_2O_7$ pyrochlore compounds: A category of potential materials for clean energy and environment protection catalysis. *J Rare Earth* 2020, **38**: 840–849.
[57] Vayer F, Decorse C, Bérardan D, *et al.* New entropy-stabilized oxide with pyrochlore structure: $Dy_2(Ti_{0.2}Zr_{0.2}Hf_{0.2}Ge_{0.2}Sn_{0.2})_2O_7$. *J Alloys Compd* 2021, **883**: 160773.

[58] Leitner J, Voňka P, Sedmidubský D, *et al*. Application of Neumann–Kopp rule for the estimation of heat capacity of mixed oxides. *Thermochim Acta* 2010, **497**: 7–13.
[59] Teng Z, Tan YQ, Zeng SF, *et al*. Preparation and phase evolution of high-entropy oxides $A_2B_2O_7$ with multiple elements at A and B sites. *J Eur Ceram Soc* 2021, **41**: 3614–3620.
[60] Liu DB, Shi BL, Geng LY, *et al*. High-entropy rare-earth zirconate ceramics with low thermal conductivity for advanced thermal-barrier coatings. *J Adv Ceram* 2022, **11**: 961–973.
[61] Luo XW, Luo LR, Zhao XF, *et al*. Single-phase rare-earth high-entropy zirconates with superior thermal and mechanical properties. *J Eur Ceram Soc* 2022, **42**: 2391–2399.
[62] Tu TZ, Liu JX, Zhou L, *et al*. Graceful behavior during CMAS corrosion of a high-entropy rare-earth zirconate for thermal barrier coating material. *J Eur Ceram Soc* 2022, **42**: 649–657.
[63] Birol H, Damjanovic D, Setter N. Preparation and characterization of $(K_{0.5}Na_{0.5})NbO_3$ ceramics. *J Eur Ceram Soc* 2006, **26**: 861–866.
[64] Lamb J, Jarvis K, Manthiram A. Molten-salt synthesis of O_3-type layered oxide single crystal cathodes with controlled morphology towards long-life sodium-ion batteries. *Small* 2022, **18**: 2106927.
[65] Paul B, Singh K, Jaroń T, *et al*. Structural properties and the fluorite–pyrochlore phase transition in $La_2Zr_2O_7$: The role of oxygen to induce local disordered states. *J Alloys Compd* 2016, **686**: 130–136.
[66] Han YJ, Yu RW, Liu HH, *et al*. Synthesis of the superfine high-entropy zirconate nanopowders by polymerized complex method. *J Adv Ceram* 2022, **11**: 136–144.